ENHANCING PERFORMANCE AND RELIABILITY OF HYBRID PV-WIND ENERGY CONVERSION SYSTEM USING FAULT ANALYSIS AND MITIGATION TECHNIQUE WITH ANN BASED DVR

Meenakshi Chouhan, Kapil Parikh, Prakash Baharni
E-Mail Id: kapilparikh@gmail.com
Department of Electrical Engineering, Shrinathji Institute of Technology & Engineering, Nathdwara. Rajasthan, India

Abstract- The major problem in renewable energy system is that the variation in power generation from time to time because of the intermittent nature of the renewable sources. In this paper presents a fault analysis, classification, and mitigation technique for a hybrid grid-connected photovoltaic (PV) wind energy conversion system (WECS) using Artificial Neural Network (ANN) based Dynamic Voltage Restorer (DVR). The proposed system aims to improve the performance and reliability of the hybrid energy conversion system during fault conditions. The study uses simulation to evaluate the effectiveness of the proposed fault analysis, classification, and mitigation technique in detecting and mitigating various types of faults in the hybrid system, such as voltage sag, voltage swell, symmetrical and asymmetrical faults. The results show that the proposed system is effective in detecting and classifying the faults accurately and mitigating them using DVR. The ANN-based fault classification algorithm provides high accuracy in identifying different types of faults, and the DVR is capable of quickly restoring the system's voltage to its nominal level. The study concludes that the proposed fault analysis, classification, and mitigation technique can significantly improve the reliability and performance of the hybrid PV-WECS system during fault conditions.
Keywords: PV, WECS, Battery, ANN, DVR.

1. INTRODUCTION

Amidst the acute depletion of fossil fuels and escalating concerns over atmospheric pollution, there is a growing global fascination with renewable energy sources such as photovoltaic (PV), wind, and hydro power. Solar and wind energy, in particular, are abundantly available worldwide. However, the intermittent nature of these renewable resources necessitates innovative solutions for consistent power generation. To address this challenge, the concept of Hybrid Renewable Energy Systems (HRES) has gained prominence. HRES involves the combination of two or more energy sources with a storage system to enhance efficiency and reduce the cost of energy production, especially in remote locations. Unlike single-source systems, remote hybrid systems demonstrate superior performance. Managing the fluctuations in generated power is crucial, and literature reveals various HRES types operating in grid-connected or stand-alone modes.

In the realm of HRES, energy management is typically achieved using a Proportional-Integral (PI) controller. This controller regulates a buck-boost bi-directional converter for battery charging and discharging, incorporating a current control strategy to maintain power balance. The conventional control strategy relies on mathematical modeling of the system. Hybrid systems emerge as effective solutions for electrical energy generation, especially in remote or micro-generation settings linked to a weak AC grid. By combining conventional and renewable energy sources through a DC bus, these systems offer versatility. In isolated areas, integrating electro-chemical storage with hybrid systems can eliminate the need for diesel generators.

This study focuses on a hybrid generation system that combines PV and wind turbines with storage batteries to overcome periods of insufficient generation and facilitate system control. Various system topologies are available, depending on the interface converters between sources and the interconnection technique. The investigation includes energy losses in power conditioning converters, optimal control, and energy management.

The primary objective of this work is to explore the proposed system is effective in detecting and classifying the faults accurately and mitigating them using DVR. The ANN-based fault classification algorithm provides high accuracy in identifying different types of faults, and the DVR is capable of quickly restoring the system's voltage to its nominal level. The study concludes that the proposed fault analysis, classification, and mitigation technique can significantly improve the reliability and performance of the hybrid PV-WECS system during fault conditions.

2. DESCRIPTION OF PROPOSED CONFIGURATION AND MODELING OF THE HRES

The Simulink model of the proposed grid connected wind PV energy conversion system is shown in the fig. 2.1. The model consists of 2MW of PV system and 2MW of wind system. The system voltage is 440V rms and grid side voltage is around 63KV RMS. The 100KW load is connected with the ANN – based DVR system which is

used to mitigate the power quality issues occurs during faulty conditions. An additional load of 50KW is connected with the system with the help of circuit breaker to analysis the system dynamic performance.

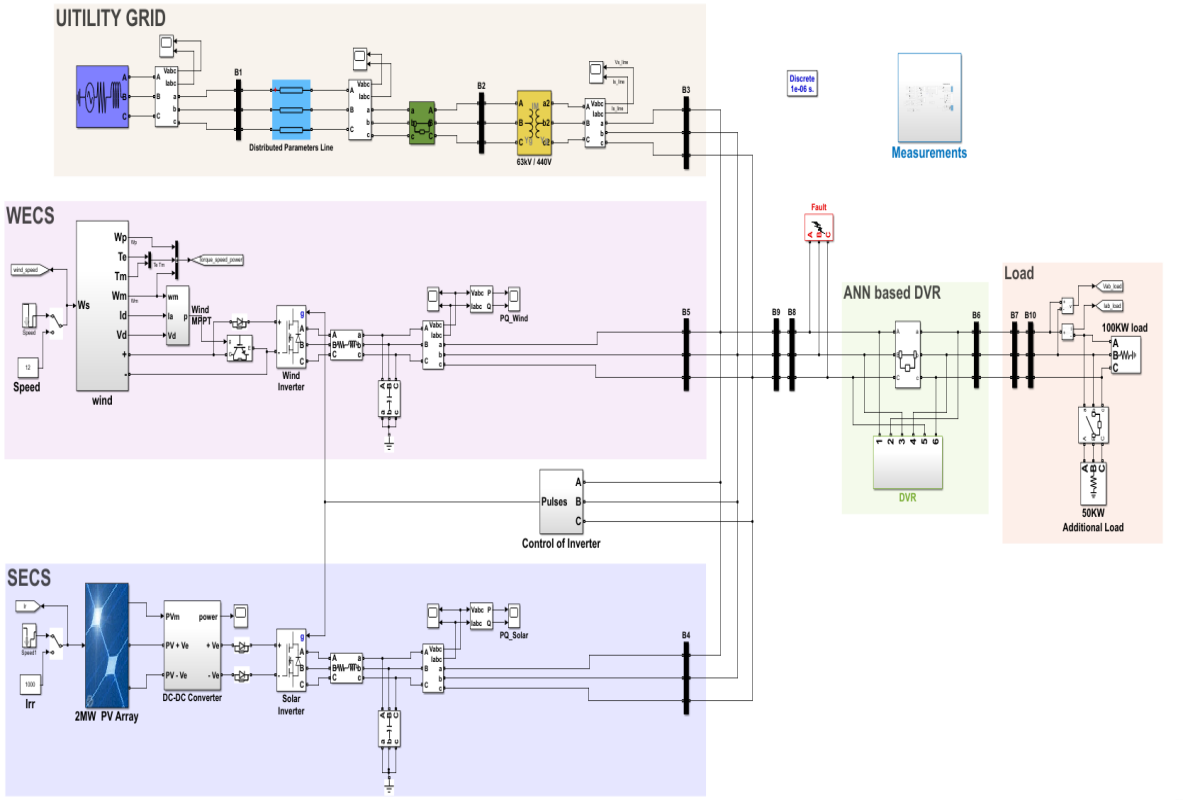

Fig. 2.1 Simulink model of the proposed grid connected wind PV energy conversion system with artificial neural network-based DVR

2.1 PV System Modeling

The equivalent circuit of a PV cell is shown in Fig. 2.2. The current source I_{ph} represents the cell photocurrent. R_{sh} and R_s are the intrinsic shunt and series resistances of the cell, respectively. Usually the value of R_{sh} is very large and that of R_s is very small, hence they may be neglected to simplify the analysis. Practically, PV cells are grouped in larger units called PV modules and these modules are connected in series or parallel to create PV arrays which are used to generate electricity in PV generation systems. The equivalent circuit for PV array is shown in Fig. 2.2.

The voltage–current characteristic equation of a solar cell is provided:

Module photo-current I_{ph}: $I_{ph} = [\, I_{SC} + K_i\,(T - 298)] * I_r\,/1000$

Here: I_{ph}: photo-current (A), I_{sc}: short circuit current (A), K_i: short-circuit current of cell at 25 °C and 1000 W/m^2, T: operating temperature (K), I_r: solar irradiation (W/m2).

Module reverse saturation current I_{rs}: $I_{rs} = I_{sc}\,/[\exp\,(qV_{oc}\,/N_S\,knT) - 1]$

Here: q: electron charge = 1.6 × 10−19C, V_{oc}: open circuit voltage (V), Ns: number of cells connected in series, n: the ideality factor of the diode, k: Boltzmann's constant, = 1.3805 × 10−23 J/K.

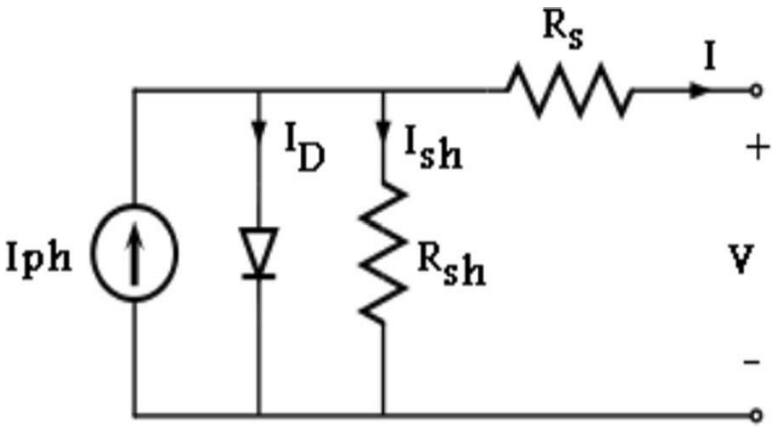

Fig. 2.2 PV cell equivalent Circuit

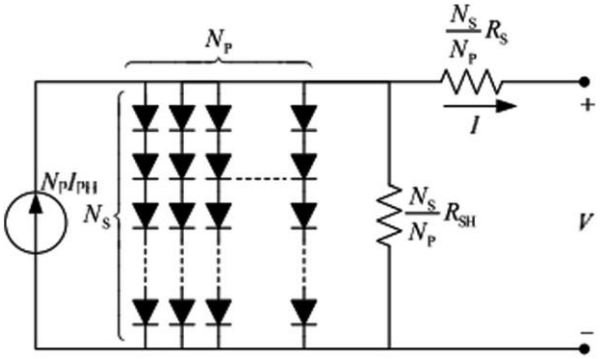

Fig. 2.3 Equivalent circuit of Solar Array

The module saturation current I_0 varies with the cell temperature, which is given by:

$$I_0 = I_{rs}\left[\frac{T}{T_r}\right]^3 \exp\left[\frac{q \times E_{g0}}{nk}\left(\frac{1}{T} - \frac{1}{T_r}\right)\right] \quad (1)$$

Here: T_r: nominal temperature = 298.15 K, E_{g0}: band gap energy of the semiconductor = 1.1 eV The current output of PV module is:

$$I = N_P \times I_{ph} - N_P \times I_0 \times \left[\exp\left(\frac{V/N_S + I \times R_S/N_P}{n \times V_t}\right) - 1\right] - I_{sh} \quad (2)$$

With $V_t = \frac{k \times T}{q}$ and $I_{sh} = \frac{V \times N_P/N_S + I \times R_S}{R_{sh}}$

Here: Np: number of PV modules connected in parallel, R_s: series resistance (Ω), R_{sh}: shunt resistance (Ω), V_t: diode thermal voltage (V).

Table-2.1 Electrical characteristics data of Sun Power SPR-305E-WHT-U Module

Name	Sun Power SPR-305E-WHT-U
Rated power (V_{mp})	305.226 W
Voltage at maximum power (V_{mp})	54.7 V
Current at maximum power (I_{mp})	5.58 A
Open circuit voltage (V_{OC})	64.2 V
Short circuit current (I_{SC})	5.96 A
Total Series-connected modules per string	11
Total Parallel strings	3
Maximum system voltage	700 V
Range of operation temperature	−40 °C to 80 °C

2.2 Wind System Modeling

The aim of the torque controller is to optimize the efficiency of capturing wind energy in a wide range of wind velocities, which retains the power generated by the machine as the optimal expressed value. It can be seen from the block diagram shown in Fig. 2.4. For any wind speed, the MPPT tool impose a torque reference accomplished of extracting maximum power. The curve T_{opt} is expressed by:

$$T_{opt} = K_{opt} * \omega_{opt}^2 \quad (3)$$

Where

$$K_{opt} = 0.5 * \rho A * \left(\frac{r_m}{\lambda_{opt}}\right)^3 * C_{P-max} \quad (4)$$

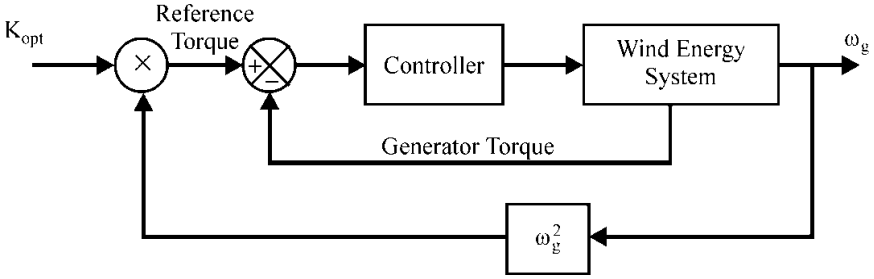

Fig. 2.4 The Block diagram of Optimal Torque control MPPT Method

The PMSG model is presented in figure. This dynamic model assumes no saturation, a sinusoidal back e.m.f. and negligible eddy current and hysteresis losses. It takes into account the iron losses and the dynamic equations for the PMSG currents are:

$$\frac{di_{md}}{dt} = \frac{1}{L_d}(v_d - R_{st}i_d + \omega L_q i_{mq}), \quad (5)$$

$$\frac{di_{mq}}{dt} = \frac{1}{L_d}(v_q - R_{st}i_q + \omega L_q i_{md} - \omega\psi_{PM}), \quad (6)$$

$$i_d = \frac{1}{R_c}(L_d \frac{di_{md}}{dt} - \omega L_q i_{mq} + R_c i_{md}), \quad (7)$$

$$i_q = \frac{1}{R_c}(L_q \frac{di_{mq}}{dt} + \omega L_d i_{md} + \omega\psi_{PM} + R_c i_{mq}), \quad (8)$$

$$i_{cd} = i_d - i_{md}, \quad (9)$$

$$i_{cq} = i_q - i_{mq}, \quad (10)$$

where i_d, i_q are the d_q axes currents, V'_d, V_q are the d_q axes voltages, i'_{cd}, i_{cq} are the d_q axes iron losses currents, i_{md}, i_{mq} are the d_q axes magnetizing currents, L_d, L_q are the d_q axes inductances, If/PM is the mutual flux due to magnets, OJ is the fundamental frequency of the stator currents, R_c is the iron losses resistance and R_{st} is the stator resistance.

The electromagnetic torque equation of the PMSG is: $T_e = \frac{2}{3} p[\psi_{PM} i_{mq} + (L_d - L_q) i_{md} i_{mq}]$ (11)

where p is the number of pole pairs.

2.3 Modeling of Batteries

The Battery block implements a basic dynamic model parameterized to be best common types of rechargeable batteries.

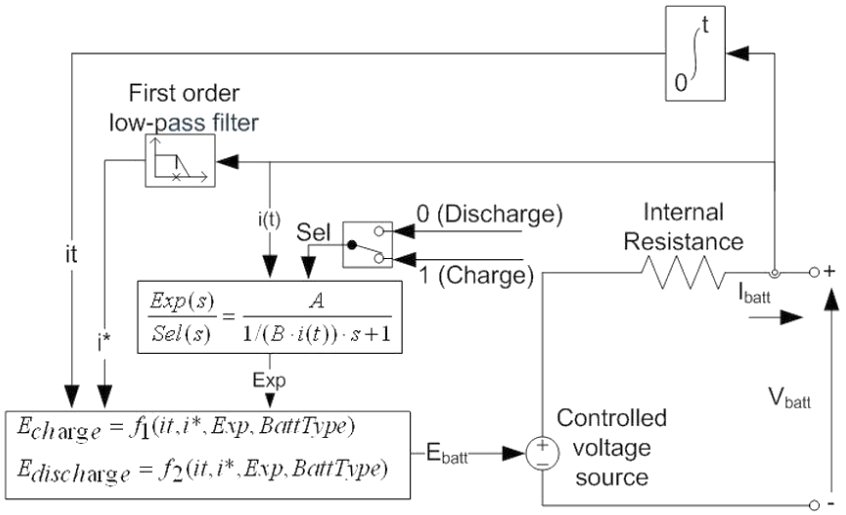

Fig. 2.5 Battery Equivalent Circuit of the Block Models

For the nickel-cadmium and nickel-metal-hydride battery types, the model uses these equations:

Discharge Model (i* > 0) $f_1(it, i*, i, Exp) = E_0 - K.\frac{Q}{Q-it}.i* - K.\frac{Q}{Q-it}.it + Laplace^{-1}\left(\frac{Exp(s)}{Sel(s)}.0\right)$

Charge Model (i* < 0) $f_2(it, i*, i, Exp) = E_0 - K.\frac{Q}{|it|+0.1.Q}.i* - K.\frac{Q}{Q-it}.it + Laplace^{-1}\left(\frac{Exp(s)}{Sel(s)}.\frac{1}{s}\right)$.

In the equations:

Here, E_{Batt} is nonlinear voltage, in V, E_0 is constant voltage, in V, Exp(s) is exponential zone dynamics, in V, Sel(s) represents the battery mode, Sel(s) = 0 during battery discharge, Sel(s) = 1 during battery charging, K is polarization constant, in Ah^{-1}, i* is low frequency current dynamics, in A, i is battery current, in A.

it is extracted capacity, in Ah. Q is maximum battery capacity, in Ah., A is exponential voltage, in V., B is exponential capacity, in Ah^{-1}.

3. SIMULATION RESULTS AND DISCUSSION

This system presents, following different Simulink studies designed to investigate the applications of the proposed control strategy with hybrid generation system in stand-alone power generation mode.

Case-1: Simulation response at constant wind speed, constant load and varying irradiance

In this case, wind speed, temperature and load are kept constant at speed of 12m/s and 25°C, 50KW respectively but irradiance is kept varying. The simulation results during asymmetrical fault, symmetrical fault are discussed below.

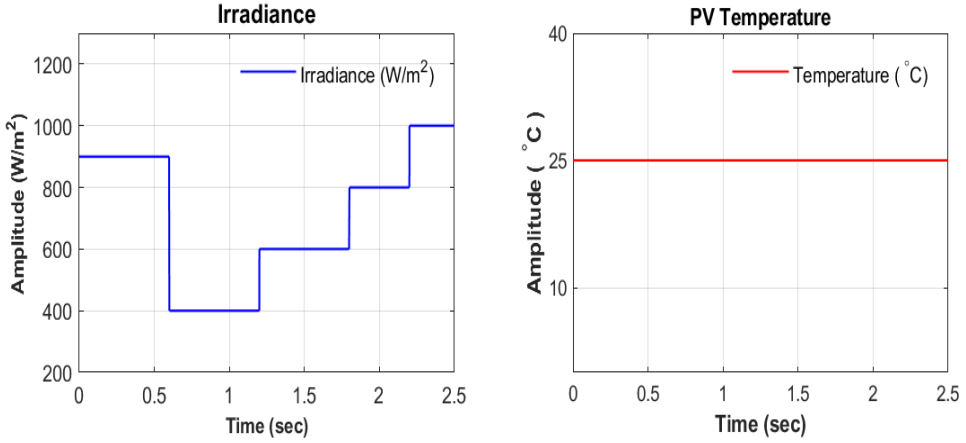

Fig. 3.1 Simulation results at constant irradiance and temperature of 1000w/m^2 & 25°C, respectively, Waveform of irradiance and temperature.

As shown in fig. 3.1, stair-case profile of irradiance is used for whole simulation time. The irradiance changes from 900w/m2 to 400w/m2 to 600w/m2 to 800w/m2 to 1000w/m2 between time duration of; t=0 to t=0.6sec, t=0.6 to t=1.2sec, t=1.2 to t=1.8sec, t=1.8 to t=2.2sec, & t=2.2 to t=2.5sec respectively. Temperature and load are kept constant for whole simulation time.

As shown in fig. 3.2, PV array voltage changes from 1157V to 514.2V to 771.3V to 1028V to 1284V and PV array current changes from 164.3A to 73.01A to 109.5A to 146.1A to 181.8A between time duration of; t=0 to t=0.6sec, t=0.6 to t=1.2sec, t=1.2 to t=1.8sec, t=1.8 to t=2.2sec, & t=2.2 to t=2.5sec respectively.

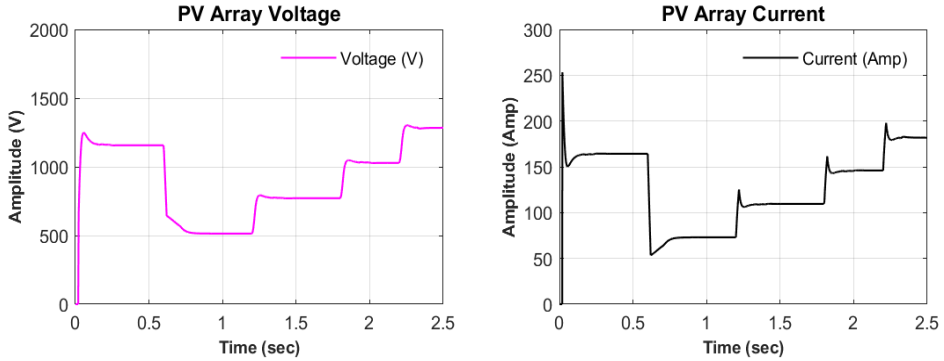

Fig. 3.2 Simulation results at constant irradiance and temperature of 1000w/m^2 & 25°C, respectively, Waveform of PV voltage and PV current.

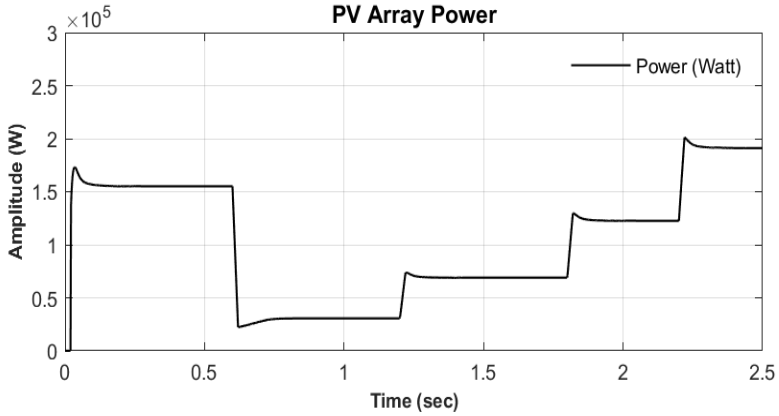

Fig. 3.3 Simulation results at constant irradiance and temperature of 1000w/m^2 & 25°C, respectively, Waveform of PV power.

As shown in fig. 3.3, PV array power changes from 155200W to 30640W to 68950W to 122600W to 192100W between time duration of; t=0 to t=0.6sec, t=0.6 to t=1.2sec, t=1.2 to t=1.8sec, t=1.8 to t=2.2sec, & t=2.2 to t=2.5sec respectively.

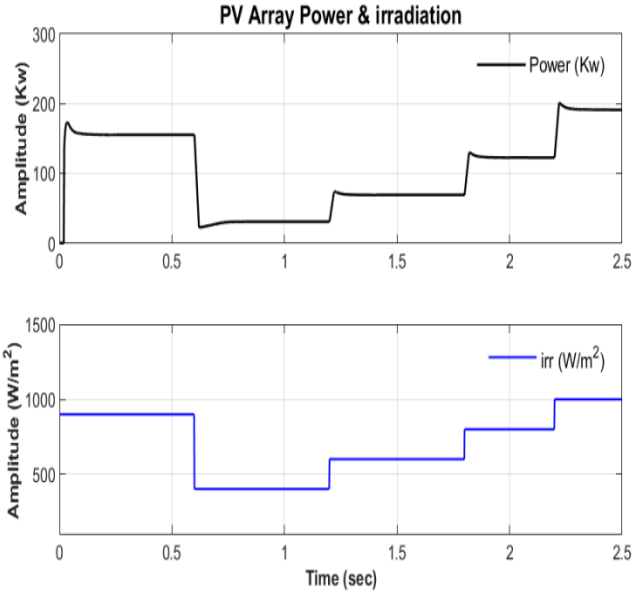

Fig. 3.4 Simulation results at constant irradiance and temperature of 1000w/m^2 & 25°C, respectively, Waveform of PV output power & irradiance.

In fig. 3.4, PV output power (in KW) is shown compared to irradiance where both changes according to change in irradiance.

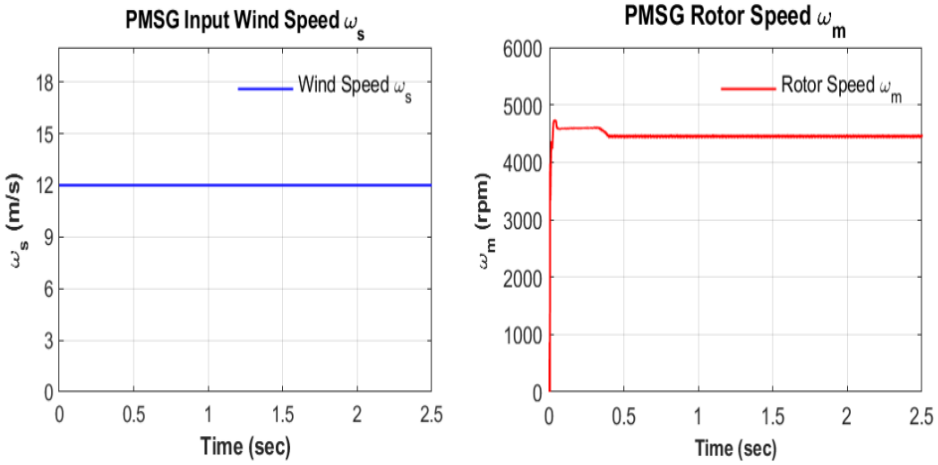

Fig. 3.5 Simulation results at constant wind speed i.e., 12m/s and load respectively, Waveform of input wind speed and Rotor speed

In fig. 3.5 Input wind speed is constant at 12m/s and PMSG rotor speed is constant at 4450RPM for whole simulation time.

Fig. 3.6 shows the output power of PMSG and PMSG Electromagnetic & Mechanical torque where they are constant at 194200W and 681N-m respectively, for whole simulation time.

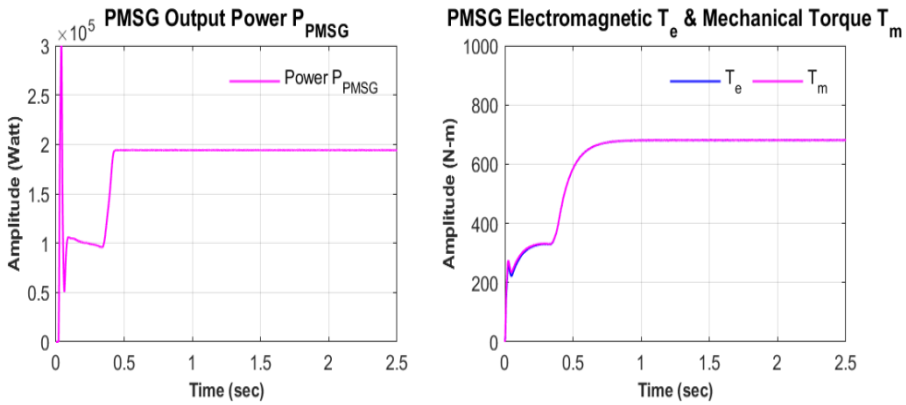

Fig. 3.6 Simulation results at constant wind speed and load, respectively, Waveform of PMSG Output Power and PMSG Electromagnetic Torque T_e & Mechanical Torque T_m

DOI Number: https://doi.org/10.30780/ specialissue-ISET-2024/049 pg. 296
Paper Id: IJTRS-ISET-24-049 www.ijtrs.com, www.ijtrs.org

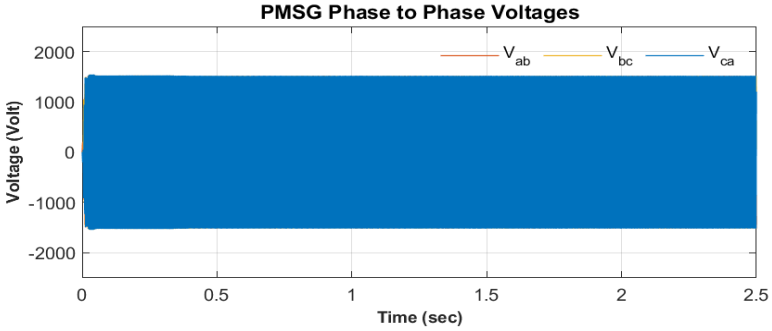

(a)

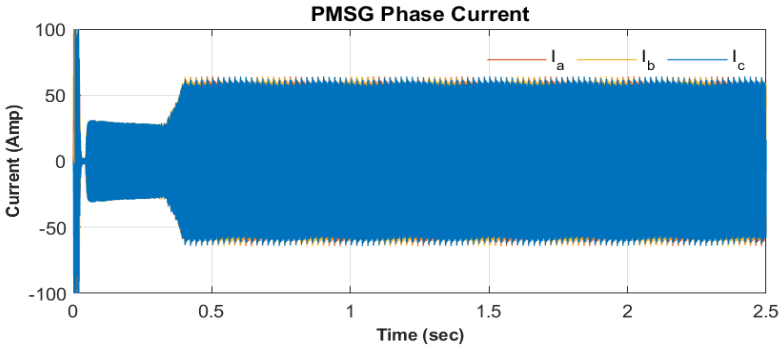

(b)

Fig. 3.7 Simulation results at constant wind speed i.e., 12m/s and load respectively, Waveform of (a) MSG phase-phase voltage (b) PMSG phase current I_{ph}

In fig. 3.7 (a) we can observe that Phase-to-phase voltage is constant at 1520V & in fig. 3.8 (b) phase current of PMSG is also constant for whole simulation time.

In fig. 3.8 the PMSG output power (in KW) is shown w.r.t. wind speed where both are constant throughout the simulation time.

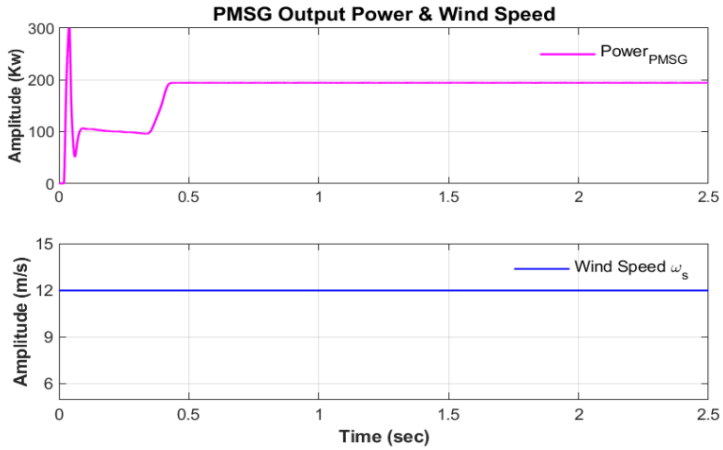

Fig. 3.8 Simulation results at constant wind speed i.e., 12m/s and load respectively, Waveform of PMSG output power and wind speed.

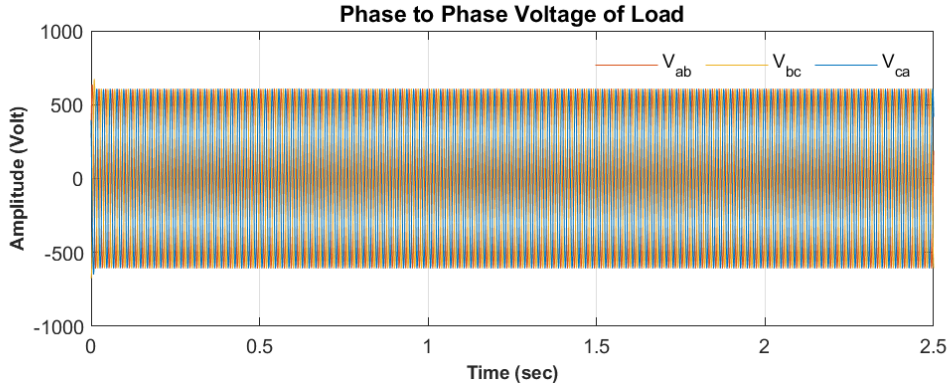

(a)

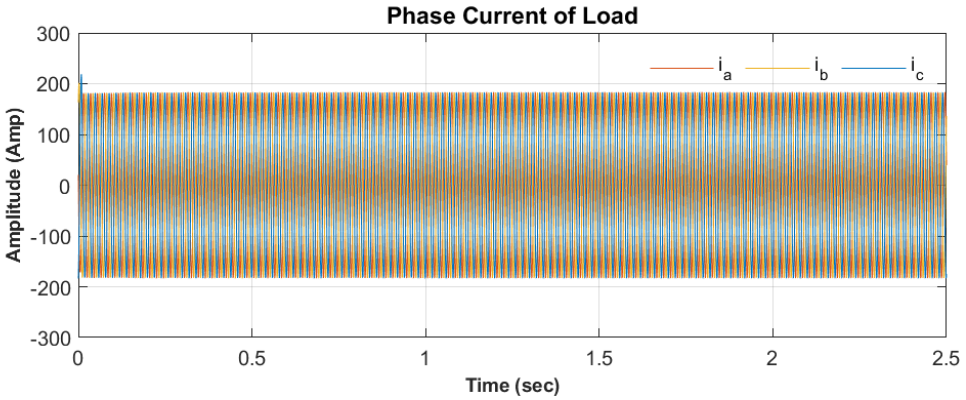

(b)

Fig. 3.9 Simulation results at constant irradiance of 1000 w/m^2, constant temperature of 25°C & wind speed 12m/s respectively, Waveform of (a) phase-phase voltage of load (b) phase current of load

In fig. 3.9 (a) & (b) we can observe that Phase-to-phase voltage and phase current of load are constant for whole simulation time.

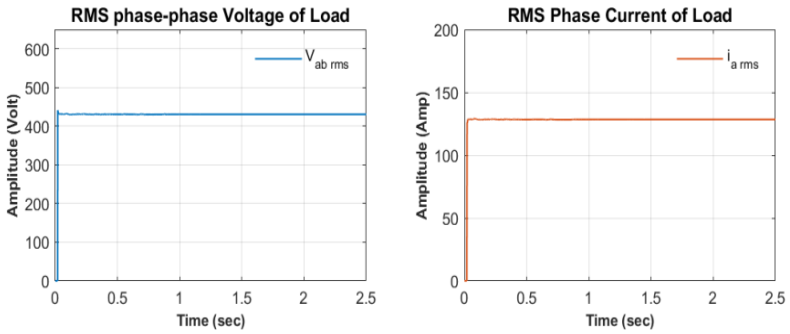

Fig. 3.10 Simulation results at constant irradiance of 1000 w/m^2, constant temperature of 25°C & wind speed 12m/s respectively, waveform of phase-to-phase RMS voltage of load and RMS phase current of Load

In fig. 3.10 both RMS phase voltage and RMS phase current are constant throughout the simulation time at 430V and 128.5A respectively.

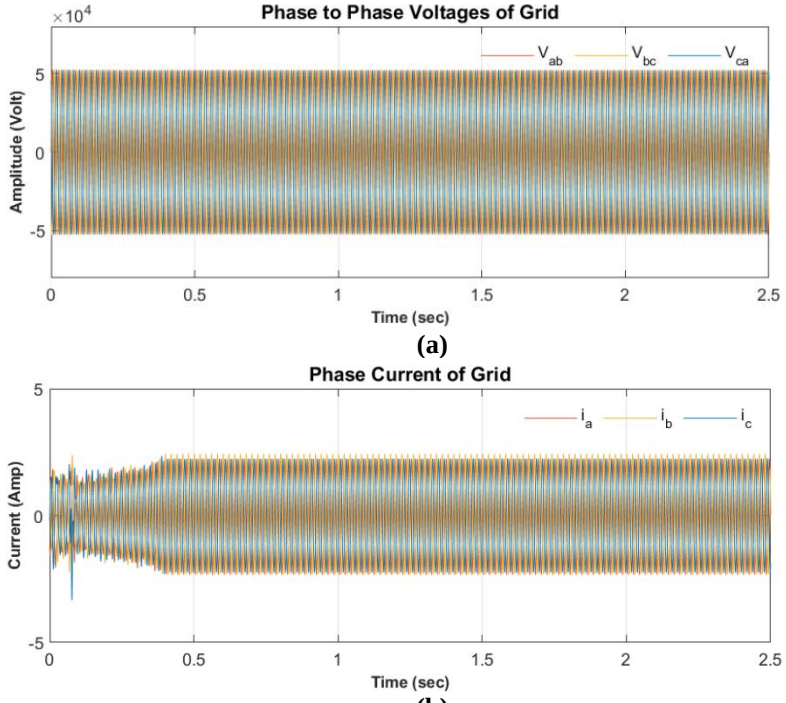

(a)

(b)

Fig. 3.11 Simulation results at constant irradiance of 1000 w/m2, constant temperature of 25°C & wind speed 12m/s respectively, Waveform of (a) phase-phase voltage of grid (b) phase current of grid

Fig. 3.11 (a) and (b) shows the grid side voltages and current respectively, which are constant for whole simulation time at 52000V & 2.3A respectively.

DOI Number: https://doi.org/10.30780/ specialissue-ISET-2024/049 pg. 298
Paper Id: IJTRS-ISET-24-049 www.ijtrs.com, www.ijtrs.org

Case 2: Simulation results during asymmetrical fault at constant wind speed, constant load and varying irradiance

The simulation results for Line-to-Line fault are shown in the following figures.

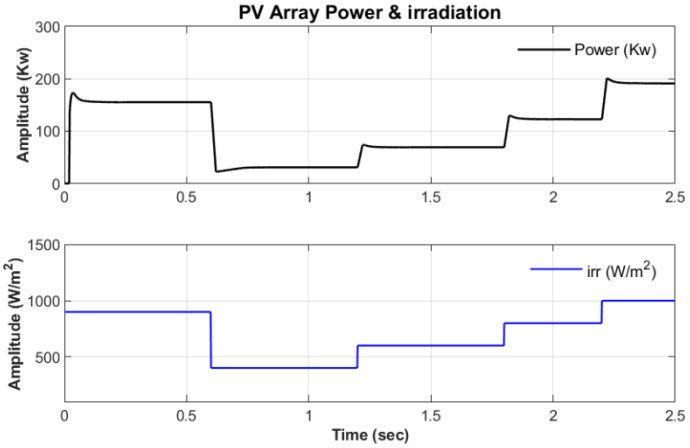

Fig. 3.12 Simulation results at constant irradiance and temperature of 1000w/m2 & 25°C, respectively, Waveform of irradiance and temperature

As shown in fig. 3.12, PV array power is shown w.r.t. irradiance. Where PV power changes from 155.2KW to 30.64KW to 68.95KW to 122.6KW to 192.1KW and irradiance changes from 900w/m2 to 400w/m2 to 600w/m2 to 800w/m2 to 1000w/m2 between time duration of; t=0 to t=0.6sec, t=0.6 to t=1.2sec, t=1.2 to t=1.8sec, t=1.8 to t=2.2sec, & t=2.2 to t=2.5sec respectively.

Fig. 3.13 shows the PMSG output power plot with respect to input wind speed which is constant at 12m/s throughout the time period, but output power is constant from t=0.5sec to t=1.2sec at 200KW, after that it decreases during line-to-line fault and again increases to reach the initial constant value at time t=1.3sec, and remain constant for remaining time period.

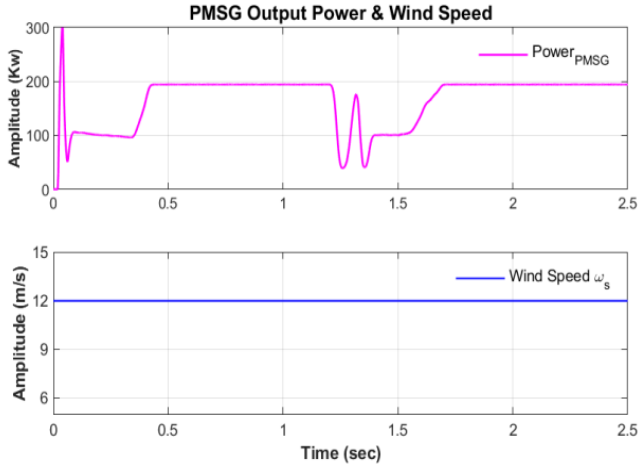

Fig. 3.13 Simulation results at constant wind speed i.e., 12m/s and load respectively, waveform of PMSG output power and wind speed

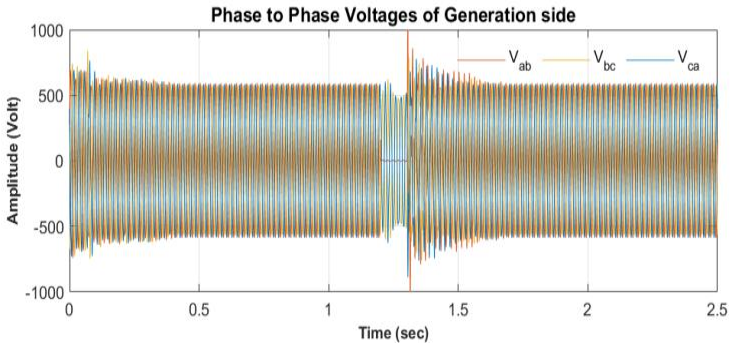

(a)

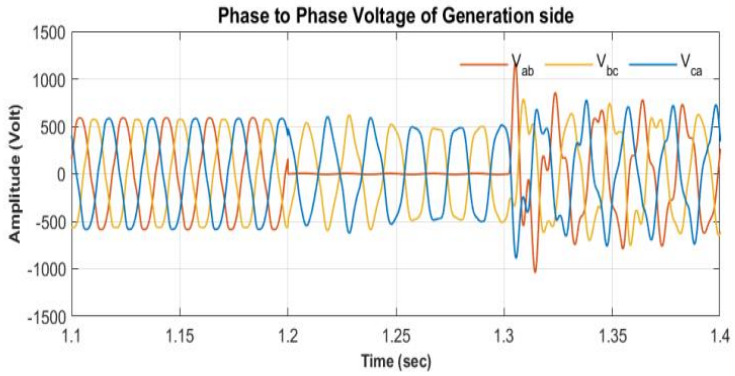

(b)

Fig. 3.14 Simulation results at constant irradiance of 1000 w/m^2, constant temperature of 25°C & wind speed 12m/s respectively, waveform of (a) phase-to-phase voltage of generation side & (b) zoom-in window of phase-to-phase voltage of generation side during line-to-line fault

According to fig. 3.14 (a) phase-to-phase voltage of generation side is constant till time t=1.2sec, after that it decreases a little due to line-to-line fault, then at t=1.3sec system gains stability and voltage again becomes constant to its initial value, which can be clearly observed in the zoom in window shown in fig. 3.14 (b).
According to fig. 3.15 (a) phase current of generation side is constant till t=1.2sec, after that it increases due to line-to-line fault, then at t=1.3sec system gains stability and current again becomes constant to its initial value, which can be clearly observed in the zoom in window shown in fig. 3.15 (b).

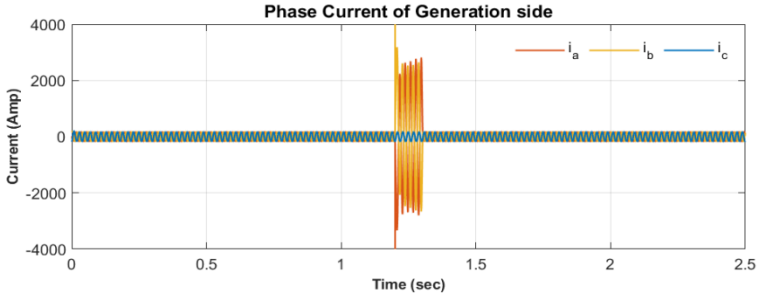

(a)

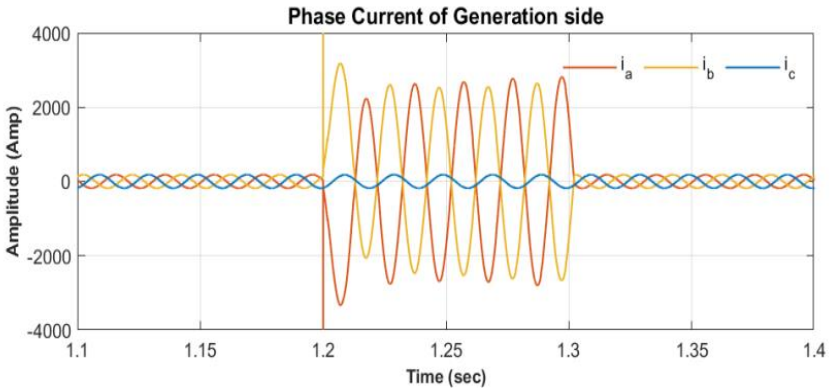

(b)

Fig. 3.15 Simulation results at constant irradiance of 1000 w/m^2, constant temperature of 25°C & wind speed 12m/s respectively, waveform of (a) phase current of generation side & (b) zoom-in window of phase current of generation side during line-to-line fault

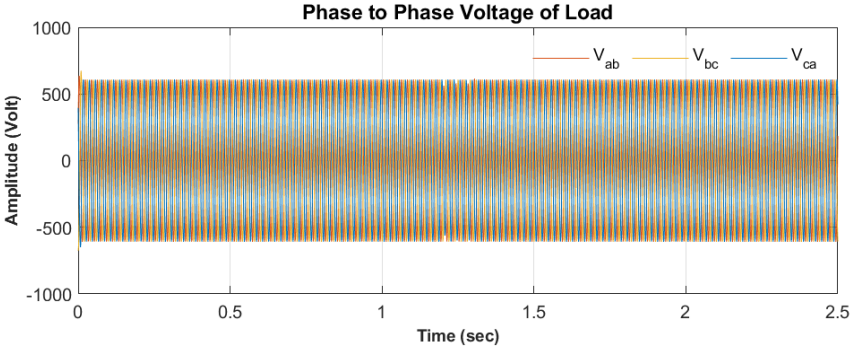

(a)

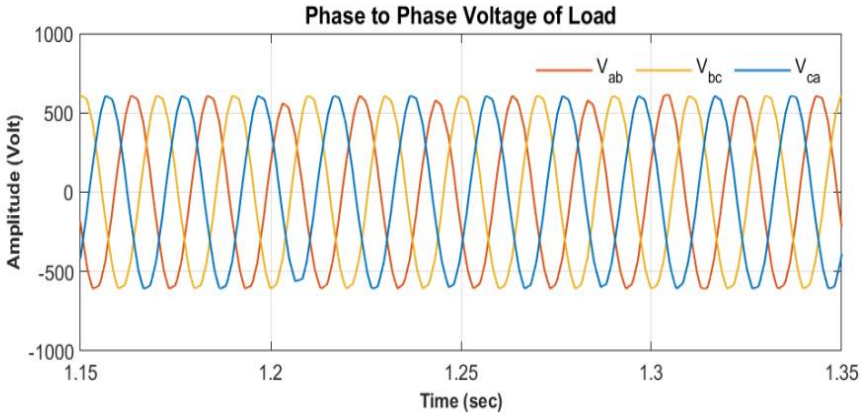

(b)

Fig. 3.16 Simulation results at constant irradiance of 1000 w/m^2, constant temperature of 25°C & wind speed 12m/s respectively, waveform of (a) phase-to-phase voltage of load side & (b) zoom-in window of phase-to-phase voltage of load side during line-to-line fault

Even during the line-to-line fault in the system, the phase-to-phase voltage of load is constant throughout the simulation time, because of the ANN tuned DVR used in the network which compensate the effect of distortions in generation side voltage to load side voltage, as shown in fig. 3.16 (a). This can also be observed in the zoom in window provided in fig. 3.16 (b) for phase voltage of load.

In fig. 3.17 (a) phase current of load is constant, it experiences a slight distortion from time t=1.2 sec to t=1.3sec which can be clearly observed in the zoom in window provided in fig. 3.17 (b).

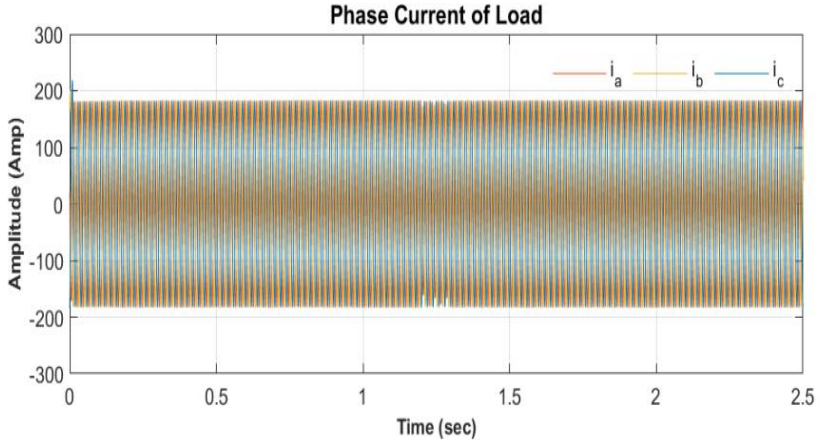

(a)

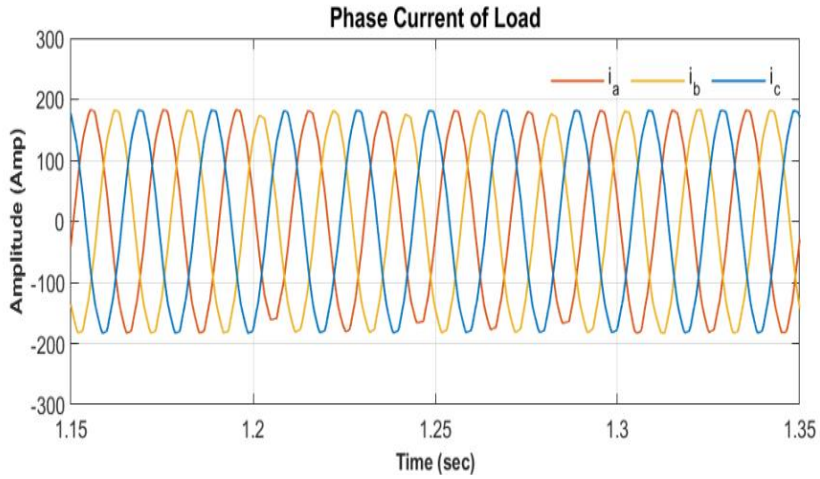

(b)

Fig. 3.17 Simulation results at constant irradiance of 1000 w/m^2, constant temperature of 25°C & wind speed 12m/s respectively, waveform of (a) phase current of load side & (b) zoom-in window of phase current of load side during line-to-line fault

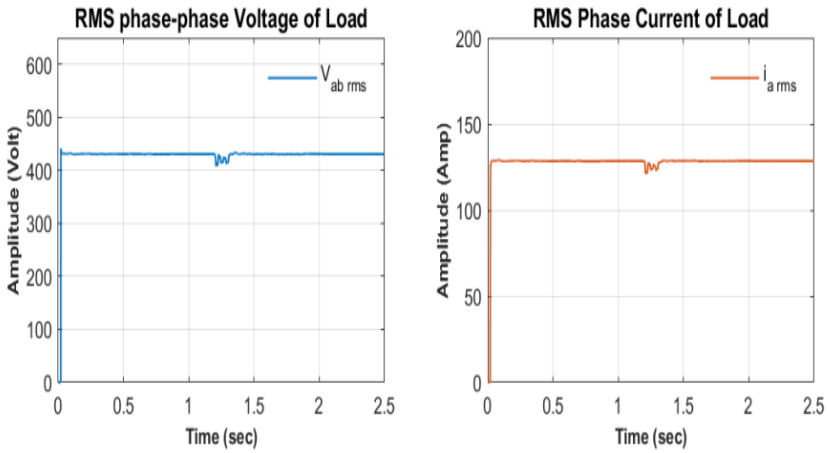

Fig. 3.18 Simulation results at constant irradiance of 1000 w/m^2, constant temperature of 25°C & wind speed 12m/s respectively, waveform of phase-to-phase RMS voltage of load and RMS phase current of load

In fig. 3.18 both RMS phase voltage and RMS phase current of load are constant throughout the simulation time at 430V and 128.5A respectively, experience slight changes when line-to-line ground fault occurs i.e., from time t=1.2sec to t=1.3sec.

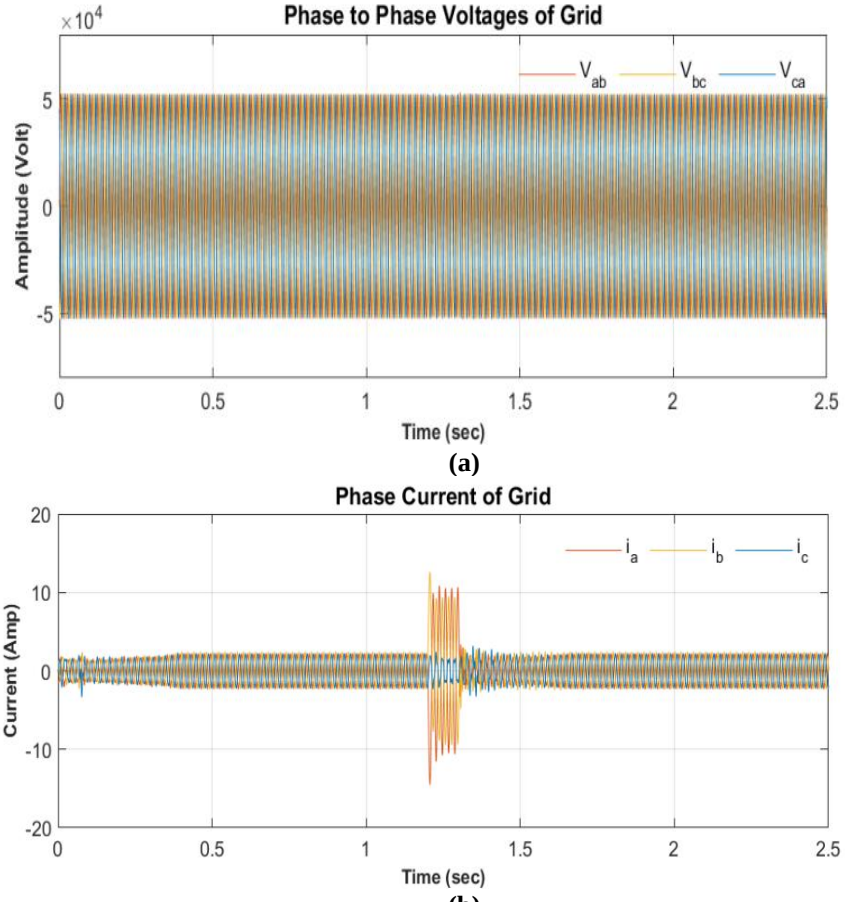

Fig. 3.19 Simulation results at constant irradiance of 1000 w/m2, constant temperature of 25°C & wind speed 12m/s respectively, Waveform of (a) phase-phase voltage of grid (b) phase current of grid during line-to-line fault

While system experience a line-to-line fault, the grid voltage does not get affected because grid is isolated from generating system by a transformer, but phase current of grid increases during the time t=1.2sec to t=1.3sec as shown in fig 3.19 (a) & (b).

In fig. 3.20 (a), we can clearly observe the distortions created by line-to-line fault which caused the Phase-to-phase voltage of generation side to decrease, but in the load side phase-to-phase voltage does not get affected due to asymmetrical fault as shown in fig. 3.20 (b), because ANN tuned DVR is used in the system which isolates the load while line-to-line fault occurs in the system.

DOI Number: https://doi.org/10.30780/ specialissue-ISET-2024/049 pg. 302
Paper Id: IJTRS-ISET-24-049 www.ijtrs.com, www.ijtrs.org

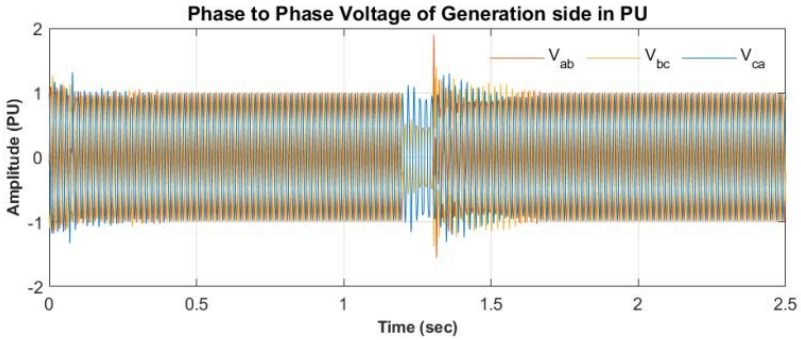

(a)

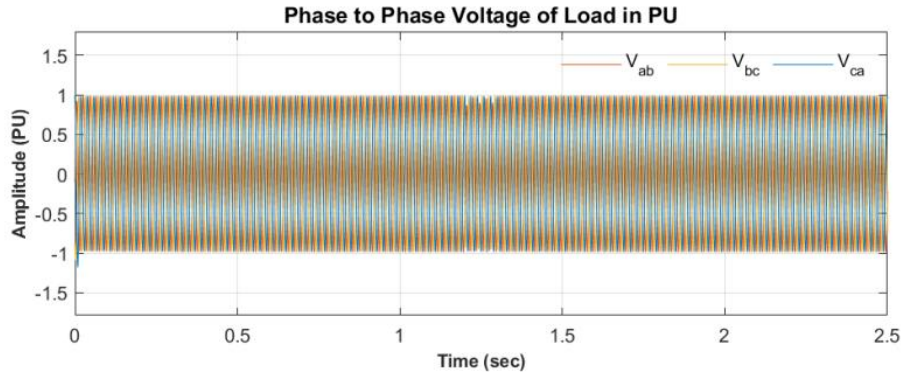

(b)

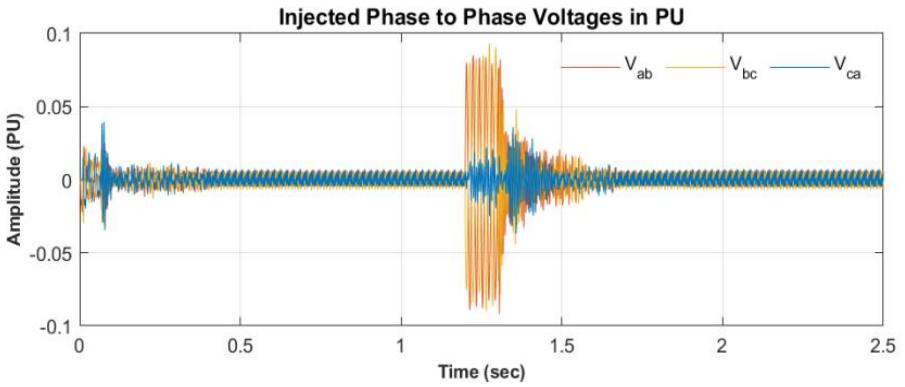

(c)

Fig. 3.20 Simulation results at constant irradiance of 1000 w/m^2, constant temperature of 25°C & wind speed 12m/s respectively, waveform of (a) phase to phase voltage of generation side (b) phase to phase voltage of load side voltage & (c) injected phase-to-phase voltage in PU

In fig. 3.20 (c) we can clearly observe that at the time of fault ANN tuned DVR inject phase voltages in load while isolating it from generation side, which assures continues phase voltage supply to the load without distortions.
In fig. 3.21 (a) and fig. 3.21 (b) phase current of generation side and phase current of load side is shown in per unit system.

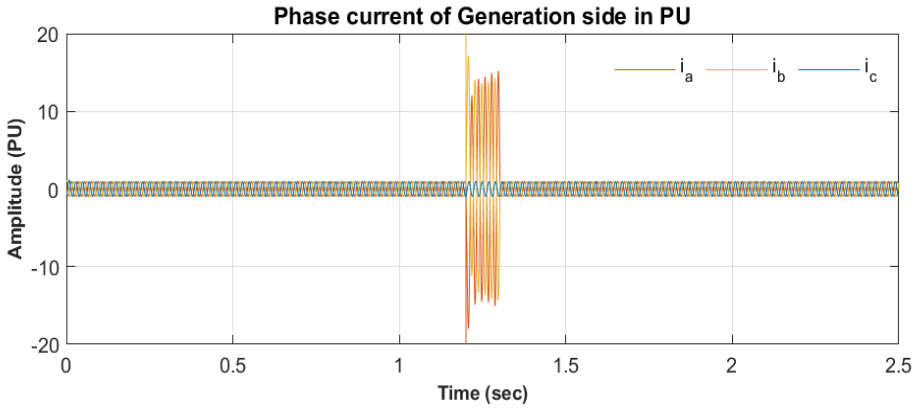

(a)

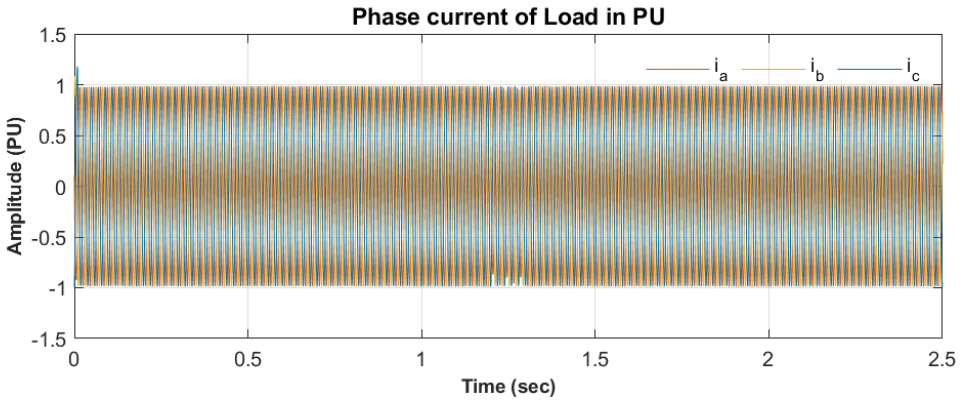

(b)

Fig. 3.21 Simulation results at constant irradiance of 1000 w/m2, constant temperature of 25°C & wind speed 12m/s respectively, waveform of (a) phase current of generation side (b) phase current of load side in PU

CONCLUSION

This paper aims to enhance the power quality of a hybrid microgrid system by addressing voltage sag and swell issues and reducing total harmonic distortion under both symmetrical and asymmetrical conditions. The primary focus is on implementing an Artificial Neural Network (ANN) based control strategy to improve voltage regulation at the DC bus (maintained within ±3.01V, meeting the ±5% standard). In comparison to conventional control strategies, the proposed ANN-based control for the Hybrid Energy Storage System (HESS) demonstrates superior responsiveness to load and generation changes, resulting in smoother power delivery and extending battery life by minimizing instantaneous current stress. The utilization of an intelligent Fuzzy Logic Controller (FLC) in the Voltage Source Inverter (VSI) ensures that the voltage output adheres to the desired level, effectively reducing harmonics distortion within the limits defined by the IEEE 519 standard. The outcomes indicate the effectiveness of the proposed system in accurately detecting and classifying faults, with Dynamic Voltage Restorer (DVR) successfully mitigating these faults. The ANN-based fault classification algorithm exhibits high accuracy in identifying various fault types, and the DVR promptly restores the system's voltage to its nominal level. In conclusion, the integrated fault analysis, classification, and mitigation technique significantly enhance the reliability and performance of the hybrid Photovoltaic-Wind Energy Conversion System (PV-WECS) during fault conditions.

REFERENCES

[1] Arul, P.G., Ramachandaramurthy, V.K. and Rajkumar, R. K., "Control strategies for a hybrid renewable energy system: A Review," Renewable and Sustainable Energy Reviews, vol. 42, pp. 597-608, 2015.

[2] Ahmed, S., Benoudjafer, C. and Benachaiba, C., "MPPT technique for standalone hybrid PV-Wind using fuzzy controller," In: Proceedings of Springer International conference on Artificial Intelligence in Renewable Energetic Systems held at Algeria during March 13-15, 2018, pp. 185-196, 2018.

[3] Alexander, A. and Thathan, M., "Modelling and analysis of modular multilevel converter for solar photovoltaic applications to improve power quality," IET Renewable Power Generation, vol. 9, pp. 78-88, 2015.

[4] Arezki, S. and Boudour, M., "Improvement of power quality for hybrid PV-FC power supply system," In: Proceedings of IEEE 16th International Power Electronics and Motion Control Conference and Exposition held at Turkey during September 21-24, 2014, pp. 725-730.

[5] Chauhan, A. and Saini, R.P., "A review on Integrated Renewable Energy System based power generation for stand-alone applications: Configurations, storage options, sizing methodologies and control," Renewable and Sustainable Energy Reviews, vol. 38, pp. 99-120, 2014.

[6] Chishti, F., Murshid. S and Singh, B. "LMMN based adaptive control for power quality improvement of grid intertie Wind-PV system," IEEE Transactions on Industrial Informatics, vol. 15, pp. 4900-4912, 2019.

[7] Chishti, F., Murshid. S and Singh, B., "Robust normalized mixed norm adaptive control scheme for PQ improvement at PCC of a remotely located Wind-Solar PV-BES Microgrid," IEEE Transactions on Industrial Informatics, vol. 16, pp. 1708-1721, 2019.

[8] Chishti, F., Murshid. S and Singh, B., "Weak grid intertie WEGS with hybrid generalized integrator for power quality improvement," IEEE Transactions on Industrial Electronics, vol. 67, pp. 1113-1123, 2020.

[9] M. Aarif; D. Joshi; R. Jangid and S.S. Sharma, "Grid Power Smoothing Management for Direct Drive PMSG Variable Speed Wind Energy Conversion System with Multilevel Converter", IEEE 7th International Conference on ICT for Sustainable Development, Organized by Global Knowledge Foundation during 29-30, July 2022 at Goa, India.

[10] Y. Joshi; J.k Maherchandani; V.K Yadav; R. Jangid; S. Vyas and S.S Sharma, "Performance Improvement of Standalone Battery Integrated Hybrid System" IEEE 7th International Conference on Electrical Energy

Systems (ICEES), Organized by Sri Sivasubramaniya Nadar College of Engineering during 11-13 Feb. 2021at Chennai, India.
[11] R. Jangid; J.k Maherchandani; R.R. Joshi and B.D Vairagi, "Development of Advance Energy Management Strategy for Standalone Hybrid Wind & PV System Considering Rural Application", IEEE 2nd International Conference on Smart Systems and Inventive Technology, Organized by Francis Xavier Engineering College during November 27-29, 2019 at Tirunelveli, India.
[12] R. Jangid; K. Parikh and P. Anjana, "Reducing the Voltage Sag and Swell Problem in Distribution System Using Dynamic Voltage Restorer with PI Controller", International Journal of Soft Computing and Engineering, ISSN: 2231-2307, Vol.-3, Issue-6, January 2014.
[13] R. Jangid; J.k Maherchandani; V.K Yadav and R.K Swami, "Energy Management of Standalone Hybrid Wind-PV System", Journal of Intelligent Renewable Energy Systems (John Wiley & Sons, Inc.) Pages 179-198, 2022.
[14] H. Kumawat and R. Jangid, "Using AI Techniques to Improve the Power Quality of Standalone Hybrid Renewable Energy Systems", Crafting a Sustainable Future Through Education and Sustainable Development, IGI Global, Pages 219-228, 2023.
[15] H. Kumawat; R. Jangid, "Performance and Investigation of Two Drive Train Interfaced Permanent Magnet Synchronous Generator for Wind Energy Conversion System", Journal of Emerging Technologies and Innovative Research, ISSN:2349-5162, Volume 7, Issue 1, January 2020.
[16] R. Jangid et. al., "Smart Household Demand Response Scheduling with Renewable Energy Resources", IEEE Third International Conference on Intelligent Computing and Control System, Organized by Vaigai College of Engineering during May 15-17, 2019 at Madurai, India.
[17] S. Kumar; R. Jangid and K. Parikh "Comparative Performance Analysis of Adaptive Neuro-Fuzzy Inference System (ANFIS) & ANN Algorithms Based MPPT Energy Harvesting in Solar PV System." International Journal of Technical Research and Science, vol. 8, Issue 3, March 2023.
[18] S. Sharma; R. Jangid and K. Parikh "Development of Intelligent Control Strategy for Power Quality Improvement of Hybrid RES Using AI Technique" International Journal of Technical Research and Science, vol. VIII, Issue II, Feb. 2023.
[19] Das, M. and Agarwal, V. 2015. "Novel high-performance stand-alone solar PV system with high gain, high efficiency DC-DC converter power stages," IEEE Transactions on Industry Applications, vol. 51, pp. 4718-4728, 2015.
[20] Faria, J., Pombo, J., Calado, M. and Mariano, S., "Power management control strategy based on artificial neural networks for standalone PV applications with a hybrid energy storage system," Energies, vol. 12, pp. 1-24, 2019.
[21] Frangieh, W. and Najjar, M. B., "Active control for power quality improvement in hybrid power systems," In: Proceedings of IEEE 3rd International Conference on Technological Advances in Electrical, Electronics and Computer Engineering held at Lebanon during April 29-30, 2015, pp. 218-223.
[22] Gayatri, M. T. L. and Parimi, A. M., "Power quality improvement of PV-WECS Microgrid using active power filter in real-time," In: Proceedings of IEEE 53rd International Universities Power Engineering Conference held at Glasgow, UK during September 4-7, 2018, pp. 1-6.
[23] Haruni, A. M. O., Negnevitsky, M., Haque, M. E. and Gargoom, A., "A novel operation and control strategy for a standalone hybrid renewable power system," IEEE Transactions on Sustainable Energy, vol. 4, pp. 402-4013, 2013.
[24] Houari, A., Djerioui, A., Saim, A., Ahmed, M. A. and Machmoum, M., "Improved control strategy for power quality enhancement in standalone systems based on four-leg voltage source inverters," IET Power Electronics, vol. 11, pp. 515-523, 2018.
[25] Hredzak, Agelidis, V. G. and Jang, M., "A Model predictive control system for a hybrid battery-ultracapacitor power source," IEEE Transactions on Power Electronics, vol. 29, pp. 1469-1479, 2014.
[26] Jayasankar, V. N. and Vinatha, U., "Implementation of adaptive fuzzy controller in a grid connected wind-solar hybrid energy system with power quality improvement features," In: Proceedings of IEEE Biennial International Conference on Power and Energy Systems: Towards Sustainable Energy held at Bengaluru during January 21-23, 2016, pp. 1-5.
[27] Kerem, A., Aksoz, A., Saygin, A. and Yilmaz, E. N., "Smart grid integration of micro hybrid power system using 6-switched 3-level inverter," In: Proceedings of IEEE 5th International Istanbul Smart Grid and Cities Congress and Fair (ICSG) held at Turkey during April 19-21, 2017, pp. 161-165.
[28] L. Jhala et al., "Development of Control Strategy for Power Management in Hybrid Renewable Energy System" International Journal of Technical Research and Science, vol. VI, Issue XII, Dec. 2021.
[29] P. S. Rajpurohit, et al., "Design of DE Optimized PI and PID Controller for Speed Control of DC Drives" International Journal of Research in Engineering, Science and Management, Volume-2, Issue-6, June-2019.
[30] N. Dhakre, et al., "Optimal Synchronization of PSS and Statcom Based Controller Using De Algorithm" International Journal for Research in Applied Science & Engineering Technology, Volume-5, Issue-XI, Nov.-2017.